

Efficient non-collinear antiferromagnetic state switching induced by orbital Hall effect in chromium

Hang Xie¹, Nan Zhang^{1,2}, Yuteng Ma^{1,3}, Xin Chen¹, Lin Ke², and Yihong Wu^{1,3}*

¹Department of Electrical and Computer Engineering, National University of Singapore, Singapore 117583, Singapore

²Institute of Materials Research and Engineering, Agency for Science, Technology and Research, Singapore 138634, Singapore

³National University of Singapore (Chong Qing) Research Institute, Chongqing Liang Jiang New Area, Chongqing 401123, China

Recently orbital Hall current has attracted attention as an alternative method to switch the magnetization of ferromagnets. Here we present our findings on electrical switching of antiferromagnetic state in Mn₃Sn/Cr, where despite the much smaller spin Hall angle of Cr, the switching current density is comparable to heavy metal based heterostructures. On the other hand, the inverse process, *i.e.*, spin-to-charge conversion in Cr-based heterostructures is much less efficient than the Pt-based equivalents, as manifested in the almost one order of magnitude smaller terahertz emission intensity and spin current induced magnetoresistance in Cr-based structures. These results in combination with the slow decay of terahertz emission against Cr thickness (diffusion length of ~11 nm) suggest that the observed magnetic switching can be attributed to orbital current generation in Cr, followed by efficient conversion to spin current. Our work demonstrates the potential of light metals like Cr as an efficient orbital/spin current source for antiferromagnetic spintronics.

Spin Hall effect (SHE) has attracted significant interest in the last decade due to its ability to convert charge current to spin current, enabling efficient electrical manipulation of magnetization dynamics of ferromagnetic layer through spin-orbit torque (SOT).¹⁻⁴ The SHE arises from both intrinsic and extrinsic scattering processes in materials with sizable spin-orbit coupling (SOC), such as heavy metals (HMs). However, recent theoretical work unveils that, other than a transverse spin current from SHE, an electric field applied along the plane of a metallic film can also induce a transverse orbital current due to orbital Hall effect (OHE).⁵⁻¹¹ Unlike the SHE, the OHE does not require SOC and therefore it was predicted to exist in a wide range of materials including light metals such as Al, Cu, and Cr.⁹⁻¹¹ Although the OHE is perceived to be more fundamental than SHE, experimental investigations on OHE are relatively recent because of primarily two reasons – difficulty in separating the two effects that typically occur concurrently in materials with the SOC and absence of direct coupling between orbital Hall current and magnetization. Nevertheless, there is increasing evidence that the OHE is present in various light metals with negligible or weak SOC,¹²⁻¹⁵ including the orbital Rashba-Edelstein effect.¹⁶⁻¹⁸ Similar to SHE, the OHE can also induce SOT,^{12-14,16} orbital Hall magnetoresistance,¹⁷ and unidirectional orbital Hall magnetoresistance¹⁹ in ferromagnet (FM)/non-magnetic metal (NM) bilayers. Notably, SOT-induced magnetization switching has been demonstrated in CoFeB/Cr without a heavy metal layer.¹³ In view of successful observation of OHE-related phenomena in HM/NM bilayers, naturally it would be of interest to understand how the orbital Hall current interacts with antiferromagnets (AFMs), which so far remains unexplored.

Among the AFMs, non-collinear AFMs, such as Mn₃Sn and Mn₃Ge, have attracted great attention recently due to their large anomalous Hall,²⁰⁻²³ anomalous Nernst,²⁴ and magneto optical Kerr effects,²⁵ which help to overcome the electrical readout difficulty faced by conventional collinear AFMs. A crucial step towards device application of non-collinear

AFMs is the realization of electrical control of the AFM magnetic order, which has been demonstrated experimentally by several groups, ranging from partial to full switching and continuous rotation of the chiral spin structure.²⁶⁻³² While most studies employ AFM/HM bilayer structures in which spin currents are generated from adjacent HM layers,^{26-30,32} recent studies have shown that the AFM order of polycrystalline Mn₃Sn can be switched by self-generated spin-polarized currents.^{31,33-35} Despite these progresses, the switching mechanism remains partially understood, such as the role of crystalline orientation^{27,30,31} and Joule heating.^{28,29} To further understand the switching mechanism and thus reduce the switching current, it is useful to explore other sources of spin current besides SHE-generated or self-induced spin current.

Here we present a study of electrical control of AFM state in Mn₃Sn/Cr bilayers, where Cr is a light metal reported to have a small SOC but a large orbital Hall conductivity (OHC).^{11,36,37} We observe efficient current-induced switching in Mn₃Sn/Cr with the switching polarity same as Mn₃Sn/Ta but opposite to Mn₃Sn/Pt, and the switching current density J_c is comparable to Mn₃Sn/Ta but less than half of Mn₃Sn/Pt. The thickness and temperature dependence study of current-induced switching further rules out the effects from interfaces and antiferromagnetic order in Cr, respectively. Similar current-induced switching results are obtained in Cr/CoFeB and Ta/CoFeB control samples, both of which exhibit same switching polarity. We further perform terahertz (THz) emission measurements in CoFeB/Cr and CoFeB/Pt and find that the THz intensity in CoFeB/Cr is much weaker than that of CoFeB/Pt under same pumping conditions. From the Cr-thickness dependence, we obtain a spin (or orbital) diffusion length of 11 nm in Cr. These results combined suggest that the current induced switching in Mn₃Sn/Cr and Cr/CoFeB is dominated by the OHE rather than SHE based mechanism.

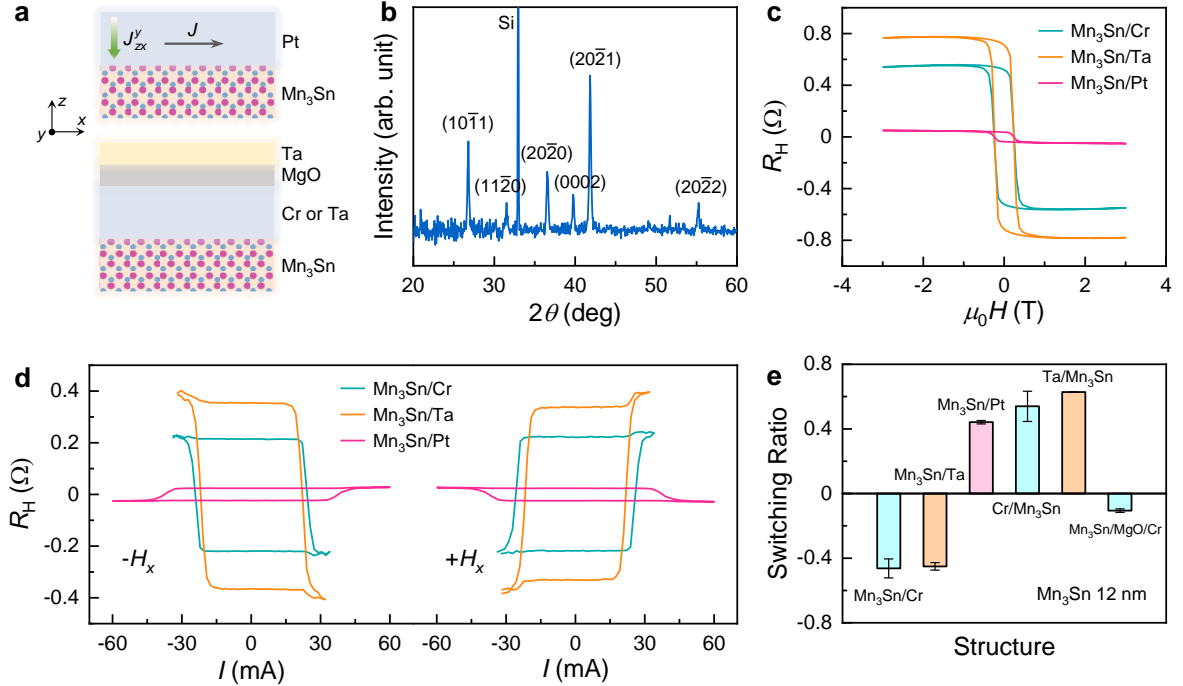


Figure 1. Structural properties of Mn_3Sn and current-induced switching in $\text{Mn}_3\text{Sn}/\text{X}$, $\text{X} = \text{Cr}$, Ta , Pt . **a**, Schematic layer structure of sample investigated. For $\text{Mn}_3\text{Sn}/\text{Cr}$ and $\text{Mn}_3\text{Sn}/\text{Ta}$ structures, additional $\text{MgO}(2)/\text{Ta}(1.5)$ capping layers (number inside the parentheses indicate thickness in nm) are used to protect the film from oxidation. The thin films are patterned into Hall bars for electrical measurements. **b**, XRD pattern of a $\text{Mn}_3\text{Sn}(60)$ coupon film. **c**, Field dependence of Hall resistance at room temperature for $\text{Mn}_3\text{Sn}(12)/\text{X}(6)$ with $\text{X} = \text{Cr}$, Ta , Pt . **d**, Current dependence of Hall resistance at room temperature for $\text{Mn}_3\text{Sn}(12)/\text{X}(6)$ with $\text{X} = \text{Cr}$, Ta , Pt , with a negative (left) and positive (right) in-plane assistant field. The current pulse width is fixed as 5 ms. **e**, Summary of switching ratio (the ratio between current and field induced Hall resistance change) of Mn_3Sn in different structures. The sign represents the switching polarity.

The schematic layer structure is shown in Figure 1a. The Mn_3Sn thin films are prepared using magnetron sputtering (see Supporting Information S1 for detailed methods). The non-magnetic metal (NM) layer X ($\text{X} = \text{Cr}$, Ta , Pt) is deposited after the annealing of Mn_3Sn to

avoid possible interdiffusion (see Supporting Information S2). Figure 1b shows the X-ray diffraction (XRD) pattern of a Mn₃Sn(60) film. Multiple peaks corresponding to (10 $\bar{1}$ 1), (11 $\bar{2}$ 0), (20 $\bar{2}$ 0), (0002), (20 $\bar{2}$ 1), and (20 $\bar{2}$ 2) planes of D0₁₉ phase Mn₃Sn are observed, confirming the polycrystalline structure in sputter-deposited Mn₃Sn. As shown in Figure 1c, all Mn₃Sn(12)/X(6) films exhibit clear AHE hysteresis loops with similar shape and coercivity, although the absolute magnitudes of AHE resistance differ from sample to sample due to different current shunting effects. The results suggest that the X layer on top of Mn₃Sn does not have much effect on the magnetic properties of Mn₃Sn.

Current-induced switching experiments are then performed using current pulses and an in-plane assistant field H_x along the current direction (see Supporting Information S5 for more details on H_x dependence). Deterministic switching behaviour is clearly observed in all the structures (Figure 1d). The switching polarity of Mn₃Sn/Ta and Mn₃Sn/Pt is consistent with the reported results and corroborates the negative and positive spin Hall angle (SHA) of Ta and Pt, respectively.^{26,30,31} Despite opposite switching polarity, both show similar switching ratio of around 45% as summarized in Figure 1e. Surprisingly, Mn₃Sn/Cr also shows evident switching loops with comparable switching ratio and critical current as Mn₃Sn/HM bilayers. We can also notice that its switching polarity is the same as that of Mn₃Sn/Ta, implying a negative SHA in Cr. We also reverse the stack deposition sequence of Mn₃Sn/Cr (see Supporting Information S3). The extracted switching ratio of Cr/Mn₃Sn together with the value of Ta/Mn₃Sn is also summarized in Figure 1e. As can be seen, similar to Ta/Mn₃Sn, Cr/Mn₃Sn has an opposite switching polarity with Mn₃Sn/Cr, whose switching ratio also increases. As standalone Mn₃Sn also shows self-induced switching behaviour (with switching ratio usually smaller than 20%), and moreover, the self-induced switching polarity of Mn₃Sn can vary depending on the underlayer due to the change in crystalline structure,³¹ we further added a thin MgO layer between Mn₃Sn and Cr layers in Mn₃Sn/Cr to exclude

dominant contribution from self-induced switching (Figure 1e and Supporting Information S4). The much-reduced switching ratio after the MgO layer insertion indicates that the switching in Mn₃Sn/Cr is mainly induced by the external orbital current from Cr layer.

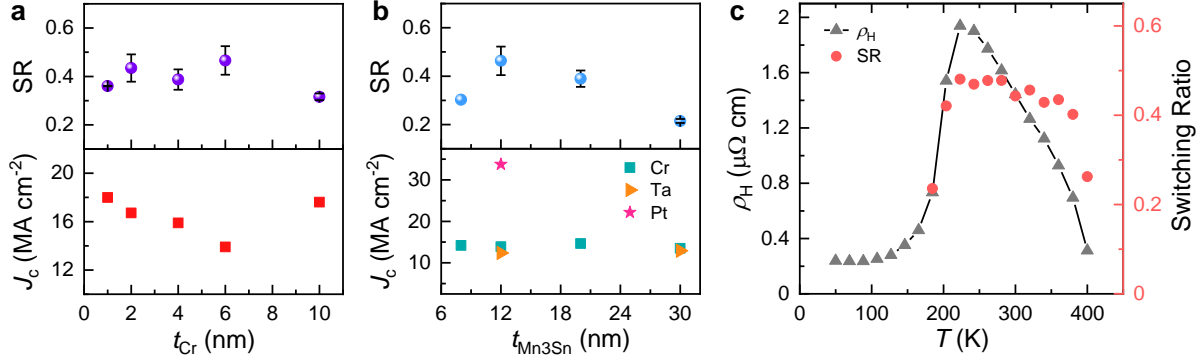


Figure 2. Cr thickness, Mn₃Sn thickness, and temperature dependence of current-induced switching in Mn₃Sn/Cr. **a**, Cr thickness t_{Cr} dependence of switching ratio and critical current density J_c in Mn₃Sn/Cr, with Mn₃Sn thickness fixed as 12 nm. The current shunting effect has been taken into consideration based on the resistivity of each layer for the estimation of current density. **b**, Mn₃Sn thickness t_{Mn3Sn} dependence of switching ratio and J_c in Mn₃Sn/Cr, with Cr thickness fixed as 6 nm. **c**, Anomalous Hall resistivity ρ_H and switching ratio of Mn₃Sn(12)/Cr(6) as a function of temperature.

To understand the mechanism of current-induced switching in Mn₃Sn/Cr, we further study the thickness dependence of current-induced switching in Mn₃Sn/Cr by varying the thicknesses of both Cr and Mn₃Sn layers. The detailed AHE and current-induced switching loops are shown in Supporting Information S6 and S7, from which the extracted switching ratio and critical current density J_c in Cr layer are plotted in Figure 2a and 2b, respectively. With varying Cr thickness t_{Cr} and fixing Mn₃Sn thickness t_{Mn3Sn} at 12 nm, the switching ratio overall is around 40%, while J_c firstly decreases from 18 MA cm⁻² to 13.9 MA cm⁻² when t_{Cr} increases from 1 nm to 6 nm and then increases back to 17.6 MA cm⁻² at $t_{Cr}=10$ nm (Figure 2a). The initial decrease of switching current density can be explained by the increased

amount of spin current generation as t_{Cr} increases, whereas the increase at 10 nm might be due to onset of self-current shunting effect when t_{Cr} exceeds a certain critical thickness (equivalent to spin diffusion length in HM). The switching ratio has a larger variation when $t_{\text{Mn}_3\text{Sn}}$ varies— increases from 30% to 46% from 8 nm to 12 nm and afterwards keeps decreasing to around 21.5% at $t_{\text{Mn}_3\text{Sn}} = 30$ nm (Figure 2b, top). The switching ratio for polycrystalline Mn_3Sn is highly sensitive to the amount and spatial distribution of crystallites with different orientations, as the switching mainly occurs when the kagome plane is parallel to the spin polarization direction.^{27,30,31} Therefore, it can vary largely with the Mn_3Sn thickness and even among samples with the same structure, due to the difference in detailed crystalline orientations. The J_c , however, shows very small variation with $t_{\text{Mn}_3\text{Sn}}$ (Figure 2b, bottom), which is distinct from the results for FM/HM bilayer where J_c increases as the magnetic layer thickness increases due to more magnetic moments needed to be switched. This may be partly caused by the heating effect as when the Mn_3Sn thickness increases more current flows in the Mn_3Sn layer, resulting in an increase of temperature in Mn_3Sn and suppression of J_c increase at large Mn_3Sn thickness.^{28,29} But, as discussed in Supporting Information S8, Joule heating should play a minor role in the present case. Nevertheless, by comparing the J_c of $\text{Mn}_3\text{Sn}/\text{Cr}$ with the values for $\text{Mn}_3\text{Sn}/\text{Ta}$ and $\text{Mn}_3\text{Sn}/\text{Pt}$, we can find that J_c of $\text{Mn}_3\text{Sn}/\text{Cr}$ is merely slightly larger than that of $\text{Mn}_3\text{Sn}/\text{Ta}$ and less than half of the $\text{Mn}_3\text{Sn}/\text{Pt}$ bilayer, indicating that Cr can induce as efficient switching in Mn_3Sn as the HM does. However, this cannot be interpreted by the conventional SHE scenario given that Cr is a 3d light metal. Furthermore, interface-related effects such as Rashba-Edelstein effect (REE) also fail to account for it, because larger switching efficiency is not observed at either smaller Cr or Mn_3Sn thickness that would lead to less current shunting effect and thus favours interfacial effect.

In addition, Cr itself exhibits an AFM ordering with a Néel temperature T_N of 311 K, which may give rise to specific spin transport phenomenon.^{36,38} Although T_N for thin film Cr can be well below room temperature, it is still prudent to vary the measurement temperature across T_N to investigate if the AFM order in Cr is relevant to the spin current generation. It is found that the switching ratio displays a plateau-like shape as a function of temperature and maintains a level above 40% from 204 K to 380 K (Figure 2c and Supporting Information S9). Clear deterministic switching with a switching ratio around 26% is observed at 400 K that is much higher than T_N of bulk Cr. The sharp drop below 204 K and above 380 K can be attributed to the disappearance of chiral AFM spin structure below the transition temperature and above Néel temperature of Mn_3Sn ^{39,40} (Figure 2c, ρ_H). Therefore, the AFM ordering in Cr is unlikely to play a role in the spin current generation in Mn_3Sn/Cr bilayers.

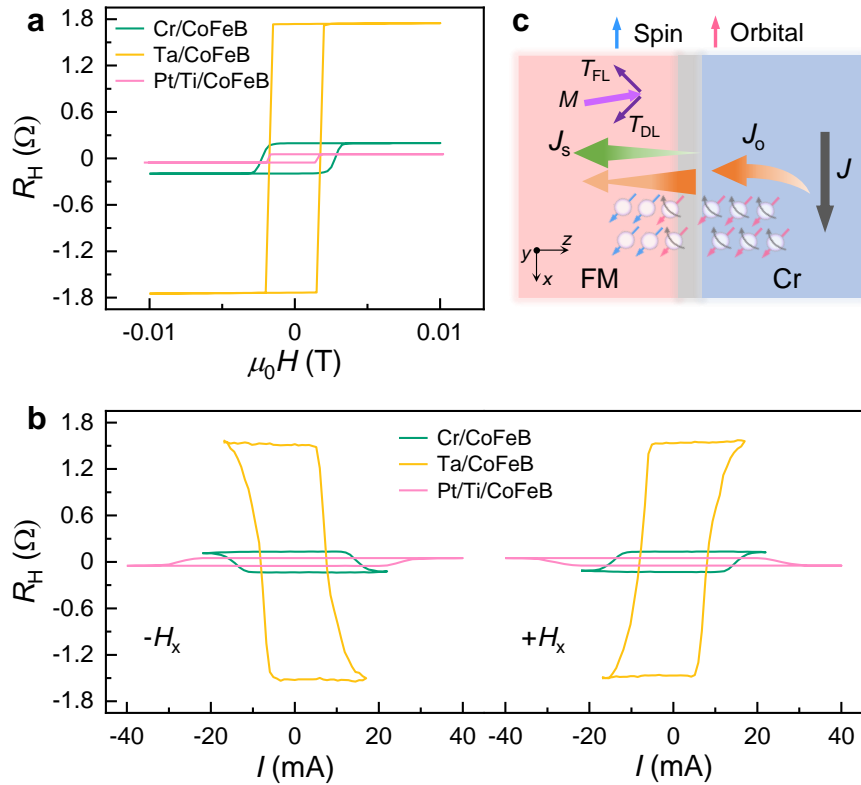


Figure 3. AHE and current-induced switching in Cr/CoFeB, Ta/CoFeB, and Pt/Ti/CoFeB. **a**, Field dependence of Hall resistance of Cr(6)/CoFeB(1.2), Ta(6)/CoFeB(1.5), and Pt(6)/Ti(2)/CoFeB(1.2). **b**, Current dependence of Hall resistance of Cr(6)/CoFeB(1.2),

Ta(6)/CoFeB(1.5), and Pt(6)/Ti(2)/CoFeB(1.2) with negative (left) and positive (right) in-plane assistant field. **c**, Schematic illustration for the OHE-induced spin current in the FM/Cr bilayers. Here, FM includes both Mn₃Sn and CoFeB, J_s and J_o are spin current and orbital current.

To examine if such phenomenon exists only in non-collinear AFMs, we further test FM-based control samples, Cr/CoFeB, Ta/CoFeB, and Pt/Ti/CoFeB, where ultrathin CoFeB layer with perpendicular magnetic anisotropy (PMA) is employed for current-induced switching measurements. The thickness of CoFeB is tailored for formation of good PMA (Figure 3a and Supporting Information S10). Since CoFeB directly grown on Pt does not show PMA, a 2 nm Ti layer is added under CoFeB for PMA formation. As shown in Figure 3b, all three structures show clear deterministic switching loops driven by applied charge current. Cr(6)/CoFeB(1.2) has the same switching polarity as Ta(6)/CoFeB(1.5) and opposite switching polarity to Pt(6)/Ti(2)/CoFeB(1.2), which is consistent with the Mn₃Sn case, indicating the spin torque switching in Mn₃Sn/Cr is rooted from Cr and can also apply to normal FM layer.

Observation of large SHA via inverse SHE voltage measurements in some 3d transition metals with small atomic number has been reported before, which was attributed to orbital filling of *d*-electrons.^{38,41} It is predicted that in addition to the spin and charge degrees of freedom, the transition metals also have orbital degrees of freedom and can generate an orbital current in a nonequilibrium state due to OHE.⁵⁻⁸ Due to the weak dependence of OHC on spin-orbit coupling, even some 3d, 4d metals and their related oxides exhibit giant values of OHC.^{5,6,8,11} Therefore, we believe the current-induced switching in Mn₃Sn/Cr can be described in a scenario of OHE from Cr. As depicted in Figure 3c, when a charge current is applied along the in-plane direction, a transverse orbital current is generated due to the OHE.

This orbital current then propagates towards the magnetic layer and is further converted to a secondary spin current at both the interface and the interior of FM via the spin-orbit coupling $\langle \mathbf{L} \cdot \mathbf{S} \rangle_{\text{FM}}$ of the magnet. Therefore, different with the SHE situation, the strength and polarization direction of the resultant spin current also rely on the sign of $\langle \mathbf{L} \cdot \mathbf{S} \rangle_{\text{FM}}$. It was previously believed that the SOC in 3d ferromagnets is weak, while recently there are increasing evidences of sizable SOT and SHA from 3d FM and AFM thin films such as Co, Fe, Ni, CoFeB and FeMn.⁴²⁻⁴⁷ Additionally, as aforementioned, spin current generation in Mn₃Sn has also been reported both theoretically and experimentally, which arises from non-collinear spin structure with SOC.^{22,31,33-35,48-52} These prerequisites allow orbital Hall current to efficiently converts to spin current when it enters Mn₃Sn or CoFeB. Regarding the polarization direction of the resultant spin current from Cr, our results are consistent with the reported results in YIG/Cr,^{38,41} Co/Cr,^{13,14} CoFeB/Cr,¹³ but opposite with the direction of Ni/Cr,^{13,14} which we consider to be related to the SOC sign in the magnetic layer because it is given by the product of the OHC sign in Cr and the SOC sign in magnetic layer, for example, the SHA is reported to be negative in Co and Fe, but positive in Ni.⁴² For Mn₃Sn, its sign of SOC is still unclear. Based on our result and the positive OHC in Cr, it can be inferred that it is negative.

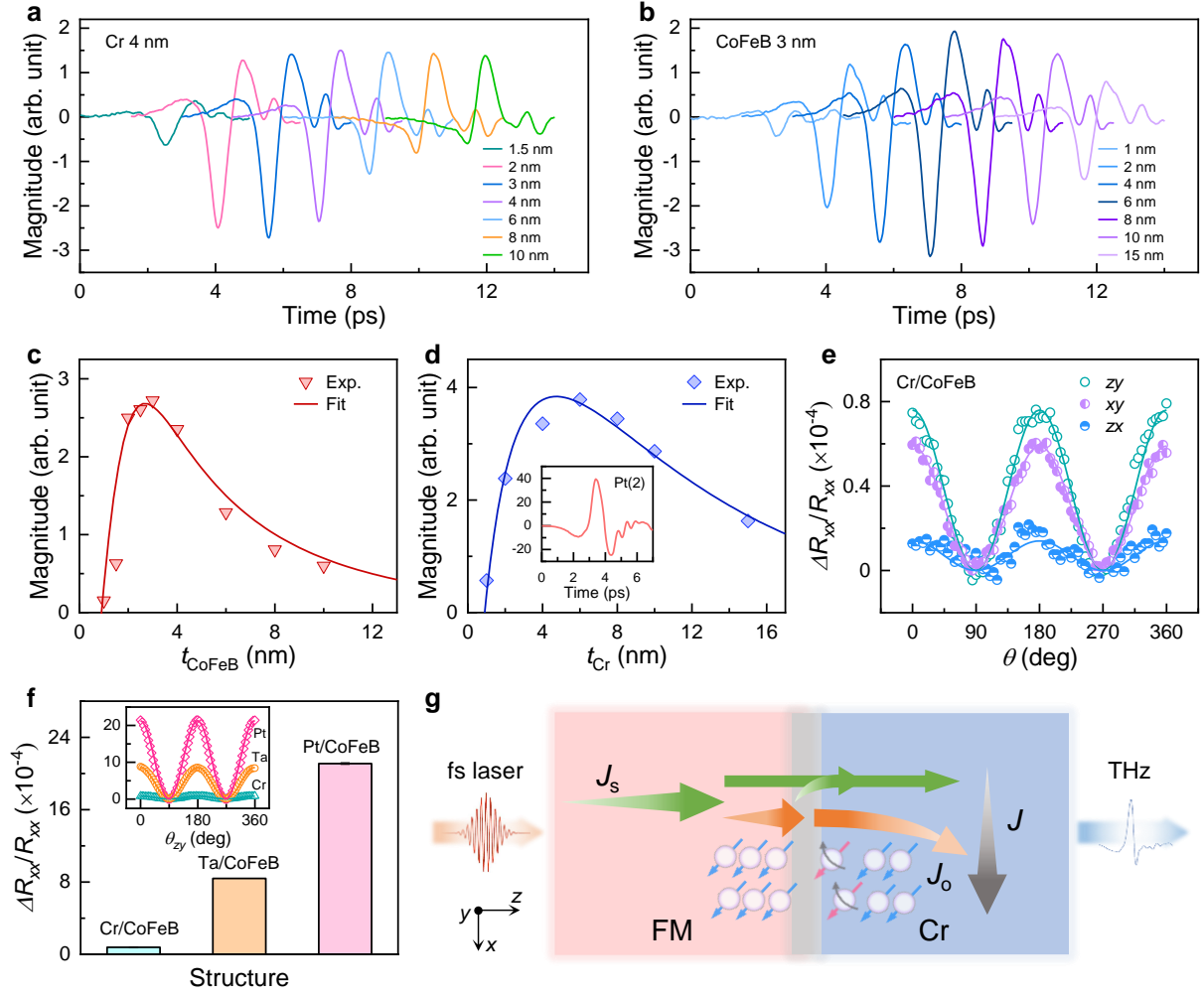


Figure 4. Cr thickness and CoFeB thickness dependence of THz waveform from CoFeB/Cr.

a, THz waveform from CoFeB/Cr at different CoFeB thickness t_{CFB} , with fixed Cr thickness at 4 nm. Waveforms are shifted in time axis for clarity. A magnetic field is applied to the sample in measurement to align the magnetization along +y direction. **b**, THz waveform from CoFeB/Cr at different Cr thickness t_{Cr} , with fixed CoFeB thickness at 3 nm. **c**, Extracted THz magnitude as a function of t_{CFB} (triangular symbol) and the fitting (solid line). **d**, Extracted THz magnitude as a function of t_{Cr} (diamond symbol) and the fitting (solid line). The inset in **d** shows THz waveform from CoFeB(3)/Pt(2). **e**, Angular dependent magnetoresistance (symbols) in Cr(6)/CoFeB(1.2) at current amplitude of 2 mA and magnetic field of 3 T with field rotated in zy, xy, zx planes. $\theta = 0$ is along z-axis for zy and zx scan and along x-axis for xy scan. Solid lines are fittings. **f**, Summary of extracted $\text{MR}(\theta_{\text{zy}})$ in Cr(6)/CoFeB(1.2),

Ta(6)/CoFeB(1.5), and Pt(6)/CoFeB(1.2). The inset in **f** shows detailed angular dependent MR curves of (Cr, Ta, Pt)/CoFeB. **g**, Schematic of THz generation in FM/Cr bilayers, which includes spin-to-orbital current conversion process.

To gain further insights of the charge-to-spin conversion mechanism in Cr-based structures, we examine its inverse process, *i.e.*, spin-to-charge conversion, through THz emission measurements. As the THz emission from Mn₃Sn is too weak to detect, possibly due to non-uniform magnetization and spin current polarization directions, we only focus on CoFeB/Cr bilayers. Figure 4a and 4b show the THz emission waveforms of CoFeB(t_{CFB})/Cr(t_{Cr}) with varied t_{CFB} and t_{Cr} , respectively. Clear THz emission has been observed throughout the thickness range with the polarity opposite to that of CoFeB/Pt, which is consistent with the electrical measurement results. Figure 4c and 4d show the corresponding t_{CFB} and t_{Cr} dependence of THz intensity. As can be seen in Figure 4c, the THz intensity initially increases from 1 nm to 3 nm, after which it decreases monotonically as t_{CFB} further increases. The thickness dependence can be fitted using^{53,54}

$$E_{\text{THz}} \propto \frac{A}{t_{\text{CFB}} + t_{\text{Cr}}} \cdot \frac{\tanh\left(\frac{t_{\text{CFB}} - t_0}{2\lambda_{\text{CFB}}}\right) \cdot \tanh\left(\frac{t_{\text{Cr}} - t_1}{2\lambda_{\text{Cr}}}\right)}{n_{\text{air}} + n_{\text{sub}} + Z_0(\sigma_{\text{CFB}}t_{\text{CFB}} + \sigma_{\text{Cr}}t_{\text{Cr}})} \cdot e^{-\frac{(t_{\text{CFB}}+t_{\text{Cr}})}{s_{\text{THz}}}}, \quad (1)$$

where A is the absorptance of the metal layers, t_0 is critical thickness of CoFeB layer, below which CoFeB layer may not show ferromagnetic properties, t_1 is the critical thickness of Cr layer, λ_{CFB} is the spin dephasing length in CoFeB, λ_{Cr} is the orbital diffusion length in Cr, n_{air} (n_{sub}) is the refractive index of air (substrate), Z_0 is the impedance of free space, σ_{CFB} and σ_{Cr} are the conductivities, and s_{THz} is the effective inverse attenuation coefficient of THz radiation in the bilayers. The values of n_{air} , n_{sub} , Z_0 , σ_{CFB} , σ_{Cr} are known: $n_{\text{air}} = 1$, $n_{\text{sub}} = 1.453$, $Z_0 = 377 \Omega$, $\sigma_{\text{CFB}} = 6.99 \times 10^5 \text{ S} \cdot \text{m}^{-1}$, $\sigma_{\text{Cr}} = 7.87 \times 10^5 \text{ S} \cdot \text{m}^{-1}$, $t_{\text{Cr}} = 4 \text{ nm}$. By further using the following parameters $t_0 = 0.9 \text{ nm}$, $\lambda_{\text{CFB}} = 0.8 \text{ nm}$, and $s_{\text{THz}} = 16 \text{ nm}$, we could fit the thickness

dependence well using Eq. (1) (Figure 4c, solid line). The fitted values of t_0 , λ_{CFB} , and s_{THz} are in good agreement with the reported value in FM/NM bilayers.⁵⁴ Similarly, by fitting the amplitude as a function of t_{Cr} using Eq. (1) (Figure 4d, solid line), we obtain the value of $\lambda_{\text{Cr}} = 11$ nm. This is comparable with reported value for Cr⁴¹ and much larger than the spin diffusion length in HM layer, which is usually around 1-2 nm.^{53,54} Besides, by comparison with the result of CoFeB/Pt bilayers (Figure 4d, inset), we find that THz amplitude in CoFeB/Cr is only 10% of CoFeB/Pt, implying much less effective spin-to-charge conversion process in CoFeB/Cr. The much weaker THz signal in CoFeB/Cr than CoFeB/HM was also reported in a previous study.⁵³

The above THz results show that despite the efficient charge-to-spin conversion in current switching experiments, FM/Cr fares much worse in the inverse process, *i.e.*, spin-to-charge conversion, compared to FM/(Pt, Ta). This is further supported by the angular dependent magnetoresistance (MR) measurements. As displayed in Figure 4e, the MR of Cr(6)/CoFeB(1.2) shows $\cos^2\theta$ relationship with θ for all three measurement configurations (see figure caption for θ definition). The angle-dependence in zy and xy scan agrees well with those of conventional FM/HM bilayers, while the MR in zx -scan shows an opposite sign (with its origin unclear at present). The MR obtained in the zy -scan corresponds to the spin Hall magnetoresistance (SMR) in FM/HM bilayers, but considering its different origin, here we call it orbital Hall MR (OMR). The extracted OMR ratio in Cr/CoFeB is around 0.79×10^{-4} , which is more than one order of magnitude smaller than the SMR ratio in Ta/CoFeB and Pt/CoFeB (Figure 4f and inset). The THz and OMR results combined suggest that SHE is not the dominant mechanism responsible for the spin current generation in FM/Cr, because otherwise, one would expect a strong THz emission and large SMR from CoFeB/Cr, as with conventional FM/HM bilayers. The sharp contrast between current-induced switching and THz/OMR results may be understood based on the OHE scenario. As aforementioned, in

current-induced switching, the OHE-induced orbital current needs to be converted to spin current at the FM/Cr interface and/or inside the FM to act on the FM layer (Figure 3c). The conversion takes place within a finite region in the FM layer near the interface, which may not affect the switching process as the torque can be generated “onsite” along with the orbital-to-spin conversion. However, this spatial separation from the generation sites of orbital current would significantly weaken the inverse process as depicted in Figure 4g. In the case of THz experiments, the inverse process, *i.e.*, spin-to-orbital conversion, is understandably inefficient due to the fast speed (v) of laser-pumping generated hot electrons (as a rule of thumb, in the case of extrinsic process, the scattering cross section is proportional to v^{-4}). This simple fact explains why the THz emission is weak in CoFeB/Cr bilayers. On the other hand, unlike the spin current that is directly reflected at the interface in FM/HM bilayer, the orbital current needs to experience extra steps of orbital-spin conversion before it can be reflected from or modulated by the magnetization direction of the FM layer and, furthermore, the whole process takes place within a finite thickness region instead of right at the interface, and therefore, the eventual reflected orbital current will be much smaller compared to spin current reflection, leading to diminishing OMR. It is worth noting that large inverse conversion efficiency has been observed previously in Cr-based ferromagnetic heterostructures in spin-pumping experiments,^{38,41} which differs from both the THz and OMR measurements in this work, as near thermal equilibrium spins are directly injected into the Cr layer and a significant portion of the spins may have been converted to orbital current at or near the interface. Further studies are required to quantify the charge-orbital-spin interconversion efficiency by combining different characterization techniques and taking into account the magnetic properties of specific materials.⁵⁵⁻⁵⁷

In conclusion, we have demonstrated electrical manipulation of non-collinear AFM state in Mn₃Sn by using 3d metal Cr as the spin current source. From combined current-

induced switching, angular-dependent MR and THz emission measurements in CoFeB/Cr, we can conclude that spin-charge interconversion in Cr is distinct from heavy metals and all experimental results converge to the OHE scenario. Our work provides an alternative way to electrically manipulate the spin states of non-collinear antiferromagnets and a method to disentangle SHE and OHE in light metals.

AUTHOR INFORMATION

Corresponding Author

* Email: elewuyh@nus.edu.sg

Author contributions

Y.W. designed and supervised the project. H.X. and Y.W. designed the experiments. H.X. conducted the sample fabrication, electrical measurement, and magnetic characterization. N.Z. performed THz emission measurement. Y.M. helped with sample fabrication. X.C. performed XRD measurement. H.X., N.Z., and Y.W. analyzed the data. All authors discussed the results. H.X. and Y.W. wrote the manuscript and all the authors contributed to the final version of manuscript.

Notes

The authors declare no competing interests.

ACKNOWLEDGEMENT

Y.W. acknowledge the funding supported by the Advanced Research and Technology Innovation Centre (ARTIC), the National University of Singapore under Grant No. A-0005947-09-00.

REFERENCES

- (1) Dyakonov, M. I.; Perel, V. I. Current-induced spin orientation of electrons in semiconductors. *Phys. Lett. A* **1971**, 35, 459-460.
- (2) Hirsch, J. E. Spin Hall Effect. *Phys. Rev. Lett.* **1999**, 83, 1834-1837.
- (3) Zhang, S. Spin Hall Effect in the Presence of Spin Diffusion. *Phys. Rev. Lett.* **2000**, 85, 393-396.
- (4) Sinova, J.; Valenzuela, S. O.; Wunderlich, J.; Back, C. H.; Jungwirth, T. Spin Hall effects. *Rev. Mod. Phys.* **2015**, 87, 1213-1260.
- (5) Bernevig, B. A.; Hughes, T. L.; Zhang, S.-C. Orbitronics: The Intrinsic Orbital Current in p-Doped Silicon. *Phys. Rev. Lett.* **2005**, 95, 066601.
- (6) Tanaka, T.; Kontani, H.; Naito, M.; Naito, T.; Hirashima, D. S.; Yamada, K.; Inoue, J. Intrinsic spin Hall effect and orbital Hall effect in 4d and 5d transition metals. *Phys. Rev. B* **2008**, 77, 165117.
- (7) Kontani, H.; Tanaka, T.; Hirashima, D. S.; Yamada, K.; Inoue, J. Giant Intrinsic Spin and Orbital Hall Effects in Sr_2MO_4 (M=Ru, Rh, Mo). *Phys. Rev. Lett.* **2008**, 100, 096601.
- (8) Kontani, H.; Tanaka, T.; Hirashima, D. S.; Yamada, K.; Inoue, J. Giant Orbital Hall Effect in Transition Metals: Origin of Large Spin and Anomalous Hall Effects. *Phys. Rev. Lett.* **2009**, 102, 016601.
- (9) Go, D.; Jo, D.; Kim, C.; Lee, H.-W. Intrinsic Spin and Orbital Hall Effects from Orbital Texture. *Phys. Rev. Lett.* **2018**, 121, 086602.
- (10) Go, D.; Lee, H.-W. Orbital torque: Torque generation by orbital current injection. *Phys. Rev. Res.* **2020**, 2, 013177.
- (11) Jo, D.; Go, D.; Lee, H.-W. Gigantic intrinsic orbital Hall effects in weakly spin-orbit coupled metals. *Phys. Rev. B* **2018**, 98, 214405.
- (12) Lee, D.; Go, D.; Park, H.-J.; Jeong, W.; Ko, H.-W.; Yun, D.; Jo, D.; Lee, S.; Go, G.; Oh, J. H.; Kim, K.-J.; Park, B.-G.; Min, B.-C.; Koo, H. C.; Lee, H.-W.; Lee, O.; Lee, K.-J. Orbital torque in magnetic bilayers. *Nat. Commun.* **2021**, 12, 6710.
- (13) Lee, S.; Kang, M.-G.; Go, D.; Kim, D.; Kang, J.-H.; Lee, T.; Lee, G.-H.; Kang, J.; Lee, N. J.; Mokrousov, Y.; Kim, S.; Kim, K.-J.; Lee, K.-J.; Park, B.-G. Efficient conversion of orbital Hall current to spin current for spin-orbit torque switching. *Commun. Phys.* **2021**, 4, 234.
- (14) Sala, G.; Gambardella, P. Giant orbital Hall effect and orbital-to-spin conversion in 3d, 5d, and 4f metallic heterostructures. *Phys. Rev. Res.* **2022**, 4, 033037.
- (15) Rothschild, A.; Am-Shalom, N.; Bernstein, N.; Meron, M. y.; David, T.; Assouline, B.; Frohlich, E.; Xiao, J.; Yan, B.; Capua, A. Generation of spin currents by the orbital Hall effect in Cu and Al and their measurement by a Ferris-wheel ferromagnetic resonance technique at the wafer level. *Phys. Rev. B* **2022**, 106, 144415.

- (16) Ding, S.; Ross, A.; Go, D.; Baldrati, L.; Ren, Z.; Freimuth, F.; Becker, S.; Kammerbauer, F.; Yang, J.; Jakob, G.; Mokrousov, Y.; Kläui, M. Harnessing Orbital-to-Spin Conversion of Interfacial Orbital Currents for Efficient Spin-Orbit Torques. *Phys. Rev. Lett.* **2020**, 125, 177201.
- (17) Ding, S.; Liang, Z.; Go, D.; Yun, C.; Xue, M.; Liu, Z.; Becker, S.; Yang, W.; Du, H.; Wang, C.; Yang, Y.; Jakob, G.; Kläui, M.; Mokrousov, Y.; Yang, J. Observation of the Orbital Rashba-Edelstein Magnetoresistance. *Phys. Rev. Lett.* **2022**, 128, 067201.
- (18) Kim, J.; Go, D.; Tsai, H.; Jo, D.; Kondou, K.; Lee, H.-W.; Otani, Y. Nontrivial torque generation by orbital angular momentum injection in ferromagnetic-metal/Cu/Al₂O₃ trilayers. *Phys. Rev. B* **2021**, 103, L020407.
- (19) Ding, S.; Noël, P.; Krishnaswamy, G. K.; Gambardella, P. Unidirectional orbital magnetoresistance in light-metal-ferromagnet bilayers. *Phys. Rev. Res.* **2022**, 4, L032041.
- (20) Chen, H.; Niu, Q.; MacDonald, A. H. Anomalous Hall Effect Arising from Noncollinear Antiferromagnetism. *Phys. Rev. Lett.* **2014**, 112, 017205.
- (21) Kübler, J.; Felser, C. Non-collinear antiferromagnets and the anomalous Hall effect. *EPL* **2014**, 108, 67001.
- (22) Zhang, Y.; Sun, Y.; Yang, H.; Železný, J.; Parkin, S. P. P.; Felser, C.; Yan, B. Strong anisotropic anomalous Hall effect and spin Hall effect in the chiral antiferromagnetic compounds Mn₃X (X = Ge, Sn, Ga, Ir, Rh, and Pt). *Phys. Rev. B* **2017**, 95, 075128.
- (23) Nakatsuji, S.; Kiyohara, N.; Higo, T. Large anomalous Hall effect in a non-collinear antiferromagnet at room temperature. *Nature* **2015**, 527, 212-215.
- (24) Ikhlas, M.; Tomita, T.; Koretsune, T.; Suzuki, M.-T.; Nishio-Hamane, D.; Arita, R.; Otani, Y.; Nakatsuji, S. Large anomalous Nernst effect at room temperature in a chiral antiferromagnet. *Nat. Phys.* **2017**, 13, 1085-1090.
- (25) Higo, T.; Man, H.; Gopman, D. B.; Wu, L.; Koretsune, T.; van 't Erve, O. M. J.; Kabanov, Y. P.; Rees, D.; Li, Y.; Suzuki, M.-T.; Patankar, S.; Ikhlas, M.; Chien, C. L.; Arita, R.; Shull, R. D.; Orenstein, J.; Nakatsuji, S. Large magneto-optical Kerr effect and imaging of magnetic octupole domains in an antiferromagnetic metal. *Nat. Photonics* **2018**, 12, 73-78.
- (26) Tsai, H.; Higo, T.; Kondou, K.; Nomoto, T.; Sakai, A.; Kobayashi, A.; Nakano, T.; Yakushiji, K.; Arita, R.; Miwa, S.; Otani, Y.; Nakatsuji, S. Electrical manipulation of a topological antiferromagnetic state. *Nature* **2020**, 580, 608-613.
- (27) Takeuchi, Y.; Yamane, Y.; Yoon, J.-Y.; Itoh, R.; Jinnai, B.; Kanai, S.; Ieda, J. i.; Fukami, S.; Ohno, H. Chiral-spin rotation of non-collinear antiferromagnet by spin-orbit torque. *Nat. Mater.* **2021**, 20, 1364-1370.
- (28) Pal, B.; Hazra, B. K.; Göbel, B.; Jeon, J.-C.; Pandeya, A. K.; Chakraborty, A.; Busch, O.; Srivastava, A. K.; Deniz, H.; Taylor, J. M.; Meyerheim, H.; Mertig, I.; Yang, S.-H.; Parkin, S. S. P. Setting of the magnetic structure of chiral kagome antiferromagnets by a seeded spin-orbit torque. *Sci. Adv.* **2022**, 8, eabo5930.
- (29) Krishnaswamy, G. K.; Sala, G.; Jacot, B.; Lambert, C.-H.; Schlitz, R.; Rossell, M. D.; Noël, P.; Gambardella, P. Time-Dependent Multistate Switching of Topological Antiferromagnetic Order in Mn₃Sn. *Phys. Rev. Appl.* **2022**, 18, 024064.

- (30) Yan, G. Q.; Li, S.; Lu, H.; Huang, M.; Xiao, Y.; Wernert, L.; Brock, J. A.; Fullerton, E. E.; Chen, H.; Wang, H.; Du, C. R. Quantum sensing and imaging of spin-orbit-torque-driven spin dynamics in noncollinear antiferromagnet Mn_3Sn . *Adv. Mater.* **2022**, 2200327.
- (31) Xie, H.; Chen, X.; Zhang, Q.; Mu, Z.; Zhang, X.; Yan, B.; Wu, Y. Magnetization switching in polycrystalline Mn_3Sn thin film induced by self-generated spin-polarized current. *Nat. Commun.* **2022**, 13, 5744.
- (32) Higo, T.; Kondou, K.; Nomoto, T.; Shiga, M.; Sakamoto, S.; Chen, X.; Nishio-Hamane, D.; Arita, R.; Otani, Y.; Miwa, S.; Nakatsuji, S. Perpendicular full switching of chiral antiferromagnetic order by current. *Nature* **2022**, 607, 474-479.
- (33) Železný, J.; Zhang, Y.; Felser, C.; Yan, B. Spin-Polarized Current in Noncollinear Antiferromagnets. *Phys. Rev. Lett.* **2017**, 119, 187204.
- (34) Ghosh, S.; Manchon, A.; Železný, J. Unconventional Robust Spin-Transfer Torque in Noncollinear Antiferromagnetic Junctions. *Phys. Rev. Lett.* **2022**, 128, 097702.
- (35) Go, D.; Sallermann, M.; Lux, F. R.; Blügel, S.; Gomonay, O.; Mokrousov, Y. Noncollinear Spin Current for Switching of Chiral Magnetic Textures. *Phys. Rev. Lett.* **2022**, 129, 097204.
- (36) Freimuth, F.; Blügel, S.; Mokrousov, Y. Anisotropic Spin Hall Effect from First Principles. *Phys. Rev. Lett.* **2010**, 105, 246602.
- (37) Go, D.; Jo, D.; Kim, K.-W.; Lee, S.; Kang, M.-G.; Park, B.-G.; Blügel, S.; Lee, H.-W.; Mokrousov, Y. Long-Range Orbital Torque by Momentum-Space Hotspots. *Phys. Rev. Lett.* **2023**, 130, 246701.
- (38) Qu, D.; Huang, S. Y.; Chien, C. L. Inverse spin Hall effect in Cr: Independence of antiferromagnetic ordering. *Phys. Rev. B* **2015**, 92, 020418.
- (39) Higo, T.; Qu, D.; Li, Y.; Chien, C. L.; Otani, Y.; Nakatsuji, S. Anomalous Hall effect in thin films of the Weyl antiferromagnet Mn_3Sn . *Appl. Phys. Lett.* **2018**, 113, 202402.
- (40) Nagamiya, T.; Tomiyoshi, S.; Yamaguchi, Y. Triangular spin configuration and weak ferromagnetism of Mn_3Sn and Mn_3Ge . *Solid State Commun.* **1982**, 42, 385-388.
- (41) Du, C.; Wang, H.; Yang, F.; Hammel, P. C. Systematic variation of spin-orbit coupling with d-orbital filling: Large inverse spin Hall effect in 3d transition metals. *Phys. Rev. B* **2014**, 90, 140407.
- (42) Wang, H.; Du, C.; Chris Hammel, P.; Yang, F. Spin current and inverse spin Hall effect in ferromagnetic metals probed by $\text{Y}_3\text{Fe}_5\text{O}_{12}$ -based spin pumping. *Appl. Phys. Lett.* **2014**, 104, 202405.
- (43) Yang, Y.; Luo, Z.; Wu, H.; Xu, Y.; Li, R.-W.; Pennycook, S. J.; Zhang, S.; Wu, Y. Anomalous Hall magnetoresistance in a ferromagnet. *Nat. Commun.* **2018**, 9, 2255.
- (44) Wang, W.; Wang, T.; Amin, V. P.; Wang, Y.; Radhakrishnan, A.; Davidson, A.; Allen, S. R.; Silva, T. J.; Ohldag, H.; Balzar, D.; Zink, B. L.; Haney, P. M.; Xiao, J. Q.; Cahill, D. G.; Lorenz, V. O.; Fan, X. Anomalous spin-orbit torques in magnetic single-layer films. *Nat. Nanotechnol.* **2019**, 14, 819-824.
- (45) Yang, Y.; Xie, H.; Xu, Y.; Luo, Z.; Wu, Y. Multistate Magnetization Switching Driven by Spin Current From a Ferromagnetic Layer. *Phys. Rev. Appl.* **2020**, 13, 034072.

- (46) Luo, Z.; Zhang, Q.; Xu, Y.; Yang, Y.; Zhang, X.; Wu, Y. Spin-Orbit Torque in a Single Ferromagnetic Layer Induced by Surface Spin Rotation. *Phys. Rev. Appl.* **2019**, *11*, 064021.
- (47) Zhang, Q.; Luo, Z.; Li, H.; Yang, Y.; Zhang, X.; Wu, Y. Terahertz Emission from Anomalous Hall Effect in a Single-Layer Ferromagnet. *Phys. Rev. Appl.* **2019**, *12*, 054027.
- (48) Kimata, M.; Chen, H.; Kondou, K.; Sugimoto, S.; Muduli, P. K.; Ikhlas, M.; Omori, Y.; Tomita, T.; MacDonald, A. H.; Nakatsuji, S.; Otani, Y. Magnetic and magnetic inverse spin Hall effects in a non-collinear antiferromagnet. *Nature* **2019**, *565*, 627-630.
- (49) Kondou, K.; Chen, H.; Tomita, T.; Ikhlas, M.; Higo, T.; MacDonald, A. H.; Nakatsuji, S.; Otani, Y. Giant field-like torque by the out-of-plane magnetic spin Hall effect in a topological antiferromagnet. *Nat. Commun.* **2021**, *12*, 6491.
- (50) Hu, S.; Shao, D.-F.; Yang, H.; Pan, C.; Fu, Z.; Tang, M.; Yang, Y.; Fan, W.; Zhou, S.; Tsymbal, E. Y.; Qiu, X. Efficient perpendicular magnetization switching by a magnetic spin Hall effect in a noncollinear antiferromagnet. *Nat. Commun.* **2022**, *13*, 4447.
- (51) Wang, X.; Hossain, M. T.; Thapaliya, T. R.; Khadka, D.; Lendinez, S.; Chen, H.; Doty, M. F.; Jungfleisch, M. B.; Huang, S. X.; Fan, X.; Xiao, J. Q. Spin currents with unusual spin orientations in noncollinear Weyl antiferromagnetic Mn₃Sn. *Phys. Rev. Mater.* **2023**, *7*, 034404.
- (52) Muduli, P. K.; Higo, T.; Nishikawa, T.; Qu, D.; Isshiki, H.; Kondou, K.; Nishio-Hamane, D.; Nakatsuji, S.; Otani, Y. Evaluation of spin diffusion length and spin Hall angle of the antiferromagnetic Weyl semimetal Mn₃Sn. *Phys. Rev. B* **2019**, *99*, 184425.
- (53) Seifert, T.; Jaiswal, S.; Martens, U.; Hannegan, J.; Braun, L.; Maldonado, P.; Freimuth, F.; Kronenberg, A.; Henrizi, J.; Radu, I.; Beaurepaire, E.; Mokrousov, Y.; Oppeneer, P. M.; Jourdan, M.; Jakob, G.; Turchinovich, D.; Hayden, L. M.; Wolf, M.; Münzenberg, M.; Kläui, M.; Kampfrath, T. Efficient metallic spintronic emitters of ultrabroadband terahertz radiation. *Nat. Photonics* **2016**, *10*, 483-488.
- (54) Torosyan, G.; Keller, S.; Scheuer, L.; Beigang, R.; Papaioannou, E. T. Optimized Spintronic Terahertz Emitters Based on Epitaxial Grown Fe/Pt Layer Structures. *Sci. Rep.* **2018**, *8*, 1311.
- (55) Xie, H.; Yuan, J.; Luo, Z.; Yang, Y.; Wu, Y. In-situ study of oxygen exposure effect on spin-orbit torque in Pt/Co bilayers in ultrahigh vacuum. *Sci. Rep.* **2019**, *9*, 17254.
- (56) Yoon, J.-Y.; Zhang, P.; Chou, C.-T.; Takeuchi, Y.; Uchimura, T.; Hou, J. T.; Han, J.; Kanai, S.; Ohno, H.; Fukami, S.; Liu, L. Handedness anomaly in a non-collinear antiferromagnet under spin-orbit torque. *Nat. Mater.* **2023**, *22*, 1106-1113.
- (57) Zhu, L.; Ralph, D. C.; Buhrman, R. A. Lack of Simple Correlation between Switching Current Density and Spin-Orbit-Torque Efficiency of Perpendicularly Magnetized Spin-Current-Generator--Ferromagnet Heterostructures. *Phys. Rev. Appl.* **2021**, *15*, 024059.